HAL
open science

Airfoil Shape Optimization of a Horizontal Axis Wind Turbine Blade using a Discrete Adjoint Solver

Ali Boudis, D Hamane, O Guerri, Annie-Claude Bayeul-Lainé

To cite this version:

Ali Boudis, D Hamane, O Guerri, Annie-Claude Bayeul-Lainé. Airfoil Shape Optimization of a Horizontal Axis Wind Turbine Blade using a Discrete Adjoint Solver. Journal of Applied Fluid Mechanics, 2023, 16 (4), pp.724-738. 10.47176/jafm.16.04.1493 . hal-03974876

HAL Id: hal-03974876

https://hal.science/hal-03974876v1

Submitted on 6 Feb 2023

HAL is a multi-disciplinary open access archive for the deposit and dissemination of scientific research documents, whether they are published or not. The documents may come from teaching and research institutions in France or abroad, or from public or private research centers.

L'archive ouverte pluridisciplinaire **HAL**, est destinée au dépôt et à la diffusion de documents scientifiques de niveau recherche, publiés ou non, émanant des établissements d'enseignement et de recherche français ou étrangers, des laboratoires publics ou privés.

Journal of Applied Fluid Mechanics, Vol. 16, No. 4, pp. 724-738, 2023.
Available online at www.jafmonline.net, ISSN 1735-3572, EISSN 1735-3645.
https://doi.org/10.47176/jafm.16.04.1493

Airfoil Shape Optimization of a Horizontal Axis Wind Turbine Blade using a Discrete Adjoint Solver

A. Boudis[1†], D. Hamane[1], O. Guerri[1] and A. C. Bayeul-Lainé[2]

[1] *Centre de Développement des Energies Renouvelables, CDER, B.P 62 Route de l'Observatoire, 16340, Bouzaréah, Alger, Algerie*
[2] *Univ. Lille, CNRS, ONERA, Arts et Metiers Institute of Technology, Centrale Lille, UMR 9014 – LMFL - Laboratoire de Mécanique des Fluides de Lille - Kampé de Fériet, F-59000 Lille, France*

†*Corresponding Author Email: a.boudis@cder.dz*

(Received August 1, 2022; accepted November 22, 2022)

ABSTRACT

In this study, airfoil shape optimization of a wind turbine blade is performed using the ANSYS Fluent Adjoint Solver. The aim of this optimization process is to increase the wind turbine output power, and the objective function is to maximize the airfoil lift to drag ratio (C_L/C_D). This study is applied to the NREL phase VI wind turbine, therefore, the S809 airfoil is used as a reference profile. First, for the validation of the applied numerical model, steady-state simulations are carried out for the S809 airfoil at various angles of attack. Then, the optimization is performed with the airfoil set at a fixed angle of attack, $AOA = 6.1°$, considering three Reynolds numbers, $Re = 3\ 10^5, 4.8\ 10^5$ and 10^6. Next, computations are performed for the fluid flow around the optimized airfoils at angles of attack ranging from 0° to 20°. The results show that (i) the lift to drag ratios of the optimized airfoils are significantly improved compared to the baseline S809 airfoil, (ii) this improvement is sensitive to the Reynolds number, and (iii) the C_L/C_D ratios are also improved for another angle of attack values. Thereafter, the optimized airfoils are used for the design of the NREL Phase VI blade and the aerodynamic performances of this new wind turbine are assessed using the open-source code QBlade. These latter results indicate that when the blades are designed with the optimized airfoils, the wind turbine aerodynamic performances increase significantly. Indeed, at a wind speed of 10 m/s, the power output of the wind turbine is improved by about 38% compared to that of the original turbine.

Keywords: CFD; Airfoil; Wind turbine blade; Aerodynamic performance; Adjoint solver; Shape optimization.

NOMENCLATURE

AoA	angle of attack	R	residual
c	chord length	Re	Reynolds number
C_D	drag coefficient	t	time
C_L	lift coefficient	T	torque
C_P	power coefficient	TSR	tip speed ratio
D	design variables	U	flow field variables
F	objective function	U_∞	free stream velocity
F_a	aerodynamic force	y^+	non-dimensional wall distance
F_x	drag force	ρ	fluid density
F_y	lift force	υ	fluid kinematic viscosity
l	blade span	Ω	angular velocity
p	pressure	k	turbulent kinetic energy
P	wind turbine power	ω	specific dissipation rate
R	rotor radius	λ	adjoint vector

1. INTRODUCTION

The depletion of fossil fuel sources and the strict laws imposed by international organizations to reduce greenhouse gas emissions have motivated several countries to develop well-defined programs for a rapid transition to renewable energy sources. Therefore, renewable energy sources use has grown

at a rapid rate in recent years, but these sources still constitute a small percentage of the world's total energy consumption. Compared to other renewable energy sources, the use of wind for power generation has increased quickly over the few past decades due to its low production costs. This kind of energy is harnessed by converting the kinetic energy of the wind into useful power using a wind turbine. Currently, two types of wind turbines are in use: the most common horizontal axis wind turbines (HAWT), whose power rating varies from a few kilowatts for small wind turbines to several megawatts for giant wind turbines, and the vertical axis wind turbines (VAWT). The wind turbine blades, on which the wind acts, are the main driving element. Therefore, their geometry has a great effect on the turbine efficiency. The blade geometry is defined by different parameters including airfoil shape, chord, thickness, and twist angle distributions along the span. When designing wind turbine blades, the airfoil shape as well as the distribution of the chord and the twist angle must be well chosen to ensure that the wind turbine produces its rated power at the rated wind speed (Khalil *et al.* 2020). The blade profiles used for early wind turbines were developed for helicopter rotors such as NACA profiles. Subsequently, the operating conditions being different, many profiles adapted to wind turbines were developed.

An overview of the design of wind turbine airfoils was presented by Timmer and Van Rooij (2003). Among the design features that were identified, a high lift to drag ratio was recognized as generally preferred and the transition had to be at the nose of the wing when approaching the stall. This development of profiles continues and now the goal is to optimize them to maximize the aerodynamic performance, decrease cut-in wind speed, reduce acoustic noise, or enhance torque. In most blade geometry optimization studies, the aim was to find the chord and twist angle distributions that maximize the rotor's aerodynamic performance (Xudong *et al.* 2009; Derakhshan *et al.* 2015; Tahani *et al.* 2017). However, the airfoil shape has a great effect on the blade aerodynamics and it can also be optimized (Perez-Blanco and McCaffrey 2013). Thereby, various numerical optimization techniques have been used to optimize the wind turbine airfoil shape. Li *et al.* (2010) suggested an optimization technique that combines the response surface method and uniform experimental design to optimize the profile of a wind turbine blade. The profile was fitted using a B-spline curve. Their numerical simulations were performed using the commercial software Fine/Turbo. Ribeiro *et al.* (2012) coupled computational fluid dynamics (CFD) simulations with optimization algorithms to design new airfoils for wind turbines. Their simulations were performed using a steady-state incompressible RANS model and a one equation turbulence model. They applied single and multi-objective genetic algorithms to optimize the airfoil, with artificial neural networks serving as surrogate models. Their results showed that using artificial neural networks reduces CPU time by about 50%. Grasso (2012) developed an optimization strategy that combines the genetic algorithm with the gradient-based method to design thick airfoils dedicated to the root area of wind turbine blades. The results showed that the applied hybrid technique has improved the accuracy and robustness of the design and reduced the computational cost. He and Agarwal (2014) employed a multi-objective genetic algorithm to improve the shape and aerodynamic characteristics of the S809 profile. Bezier curves were used to parameterize the profiles, and numerical simulations were performed using the Fluent software. Their results showed a significant enhancement in lift coefficient and lift to drag ratio compared to the baseline S809 profile. Chen *et al.* (2016) used Taylor high order polynomial series to develop a new parametric representation function for profiles. The optimal model was created by coupling the genetic algorithm (GA) and the flow solver RFOIL. Their numerical results were confirmed by wind tunnel experiments. They showed that the new wind turbine profiles family has higher aerodynamic characteristics. Dhert *et al.* (2017) used a RANS model and an adjoint method to develop an aerodynamic shape optimization framework that optimizes the blade of an NREL phase VI wind turbine. The considered optimization variables were the airfoil shape, the blade twist, and the pitch angle. The optimization problem was solved for five different wind speeds. Their results showed that the averaged torque was improved by 22.1%. Schramm *et al.* (2018) considered the optimization of the airfoil shape using a CFD tool and the continuous adjoint approach. Their study aimed to examine the effect of adjoint turbulence assumption on the final shape of the airfoil. These computations were applied to NACA 0012 profile at a fixed angle of attack of 2° and 12°, and to DU 93-W-210 profile at an angle of attack of 2°. A Reynolds number of $2\ 10^6$ was used in all simulations. Their results were compared with the frozen turbulence assumption. Li *et al.* (2018) adopted the sequential quadratic programming (SQP) methodology to design new airfoils for vertical axis wind turbines. Their main objectives were to increase the maximum lift coefficient and the lift to drag ratio, and to achieve gentle stall characteristics. Akram and Kim (2021) coupled the parametric section (PARSEC) and the class shape transformation (CST) with a genetic algorithm (GA) to optimize the S809 profile. An in-house MATLAB code coupled with XFOIL was used to determine the aerodynamic characteristics of the profile. The lift coefficient and the lift to drag ratio of the airfoil optimized through CST increased by 11.8% and 9.6%, respectively, compared to the original S809. Day *et al.* (2021) proposed a semi-transient optimization process to optimize a vertical axis wind turbine blade using Adjoint Solver. To reduce the computational cost, a single blade model was used and a variable inlet velocity was employed to simulate the blade relative velocity. The optimized blade geometries were used to design improved VAWTs. Their study was applied to a reference wind turbine with a tip speed ratio (TSR) of 4.5. The best improvement in the average power coefficient was 3.5%, compared to the reference turbine. Other aerodynamic optimization studies using the Adjoint method could be cited, however, they have been

applied to aircraft, vehicle aerodynamics, high speed trains or airfoils in inviscid compressible flows. Among them, Munoz-Paniagua *et al.* (2015) used ANSYS Fluent Adjoint Solver to minimize drag force on the front of a high speed train exposed to a headwind. Kamali-Moghadam *et al.* (2020) presented a new Adjoint approach based on the inviscid compressible lattice Boltzmann method for optimizing the supercritical SC(2)0410 Airfoil shape. Their optimization objective was to reduce drag and remove shock waves on the supercritical airfoil surface with the constraint of a fixed lift. Their results that were validated through experiments in a transonic wind tunnel, showed that the used method is appropriate for supercritical airfoil optimization to remove shock and reduce wave drag. Li *et al.* (2021) applied Adjoint Solver in STAR CCM+ to optimize the head shape of a high-speed maglev train with the aim of reducing the drag force. According to their results, the improved train design reduced its aerodynamic resistance by around 4.8% when it faces into wind.

In summary, this review shows that (i) wind turbine airfoil optimization is promising for the continuous development of wind turbines, (ii) most studies were based on the use of Genetic Algorithms, and (iii) the use of Adjoint Solver to optimize the airfoil shape of a wind turbine blades has not been extensively investigated. In addition, to the best of the authors' knowledge, the Fluent Adjoint Solver was not applied to optimize the airfoil of a horizontal axis wind turbine blade. Therefore, the Fluent Adjoint Solver is applied in the current study to optimize the airfoil form of a horizontal axis wind turbine blade that is based on a non-symmetrical airfoil. Moreover, the influence of the flow Reynolds number on the final optimized airfoil is investigated, and the aerodynamic characteristics of the optimized airfoils are assessed for a wide range of angles of attack. The goal of this optimization study is to improve the performance of the wind turbines, then, the expected output of a wind turbine built with the optimized airfoils is thereafter computed.

These investigations are applied to the NREL phase VI wind turbine. First, the S809 airfoil is used as a reference profile and, using the CFD code ANSYS Fluent, numerical optimizations are carried out at an angle of attack equal to 6.1°. Three Reynolds numbers are considered, Re = $3\ 10^5$, $4.8\ 10^5$ and 10^6. Then, the lift and drag coefficients of the optimized airfoils are evaluated for angles of attack ranging from 0° to 20°. Subsequently, the original S809 airfoil of the NREL Phase VI blade is replaced by an optimized airfoil, and the output power of the new wind turbine is evaluated using the open-source code QBlade.

2. PROBLEM DESCRIPTION

Wind turbine performances are greatly influenced by the profile of the blades. Indeed, the action of the fluid (air) on the blades results in an aerodynamic force $\vec{F}_a$ and a moment that causes the blades to rotate. This force is generated by the pressure gradient between the suction and pressure sides of the blade and the friction force with the air. The aerodynamic force $\vec{F}_a$ is usually decomposed into a lift force, normal to the direction of the flow and a drag force, parallel to the direction of the flow. The drag force is the sum of the friction force and the pressure force component along the direction of the flow. The two forces are defined as follows:

$$F_y = \frac{1}{2} \cdot \rho \cdot C_L \cdot c \cdot l \cdot U_\infty^2 \tag{1}$$

and

$$F_x = \frac{1}{2} \cdot \rho \cdot C_D \cdot c \cdot l \cdot U_\infty^2 \tag{2}$$

where ρ is the density of the fluid, c is the chord of the airfoil, l is the span of the blade, U_∞, is the free-stream velocity, and C_L and C_D are the aerodynamic characteristics coefficients of the airfoil which vary with the Reynolds number of the flow, the angle of attack and the shape of the airfoil.

The rotation of the blades results in a mechanical torque $\vec{C}$ and power P which are recovered from the shaft, whose rotation is driven by the blades:

$$\vec{C} = \vec{F}_a \times \vec{r} \quad \text{and} \quad P = \vec{C} \cdot \vec{\Omega} \tag{3}$$

where $\vec{r}$ is the radial vector and $\vec{\Omega}$ is the rotational speed.

Wind turbine performances are usually represented by the wind turbine characteristic curve C_P (TSR) that depicts the variation of the power coefficient (C_P) versus the tip speed ratio (TSR) defined as:

$$TSR = \frac{r\Omega}{U_\infty} \tag{4}$$

$$C_P = \frac{P}{\frac{1}{2}\rho\pi r^2 {U_\infty}^3} \tag{5}$$

where r is the rotor radius.

Blade element momentum theory is the most common method applied to estimate wind turbine performances that increase with C_L and C_L/C_D ratio.

Different techniques based on passive or active flow control can be applied to enhance the aerodynamic characteristics of blade airfoils. Other approaches consist in modifying the geometry of the profile. The purpose of this study is to increase C_L/C_D ratio by modifying the shape of the airfoil.

3. AIRFOIL OPTIMIZATION

The optimization problem consists to find the design parameters that control the geometry of the airfoil, to maximize the objective function F that is related to both geometric design variables, D, and flow field variables, U. This maximization is subject to the constraint that the boundary conditions and the flow equations are all satisfied.

Consequently, the optimization problem is formulated as follows:

Maximize: $\mathrm{F(U(D), D)}$

$$\text{subject to:} \begin{cases} R(U(D), D) = 0 \\ \alpha = \alpha_0 \\ c = c_0 \end{cases} \tag{6}$$

where R is the residuals of the Navier-Stokes equations, α is the angle of attack (AoA).

The objective function F in this study is the lift to drag ratio, C_L/C_D and the design variables D are the grid points that define the airfoil coordinates.

Figure 1 shows an overview of the Adjoint Solver optimization procedure. The first step of the optimization method is to compute the flow field using the flow solver. Then, the Adjoint Solver uses the solution to calculate the sensitivity gradients of the observed variable at each node on the airfoil surface. Based on the calculated sensitivity field, the airfoil geometry is modified and its surrounding mesh is actualized by the morphing tool. Then, the flow solver is used to calculate the flow field over the modified airfoil and to evaluate the new airfoil lift to drag ratio. The optimization cycle is an iterative process that stops when the objective function is achieved or if a predefined maximum number of iterations is reached.

3.1. Fluid Equations

The governing equations of the fluid flow around the airfoil are the steady-state, incompressible Reynolds Averaged Navier-Stokes equations (RANS equations) which are written in tensor notation as follows:

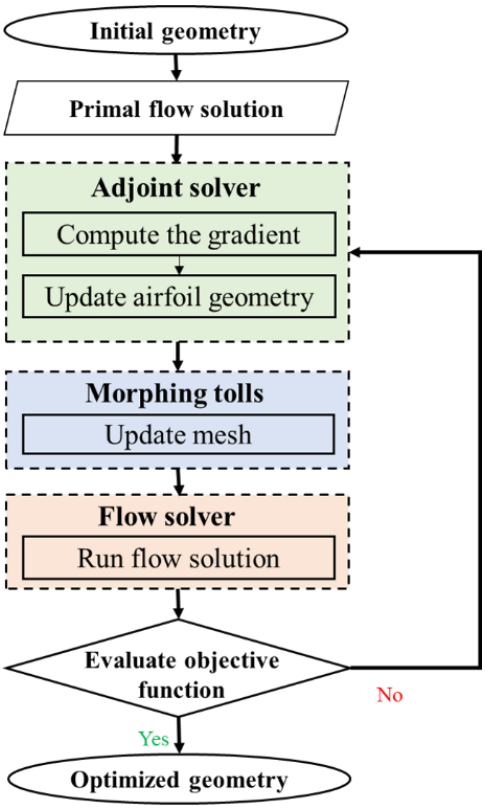

Fig. 1. Aerodynamic shape optimization based on CFD and Adjoint Solver.

$$\frac{\partial \bar{u}_i}{\partial x_i} = 0 \tag{7}$$

$$\bar{u}_j \frac{\partial \bar{u}_i}{\partial x_j} = \frac{-1}{\rho}\frac{\partial \bar{p}}{\partial x_i} + \frac{\partial}{\partial x_j}\left(\upsilon \frac{\partial \bar{u}_i}{\partial x_j} - \overline{u_j' u_i'}\right) \tag{8}$$

where $\bar{u}_i$ is the ith component of the average velocity vector, $\bar{p}$ represents the average pressure, υ is the kinematic viscosity of the fluid, u_j' and u_i' are the fluctuating velocity components and $\overline{u_j' u_i'}$ is the Reynolds-stress tensor.

The solution of equations (7) and (8) requires the use of a closure model that allows the calculation of turbulence stresses from the mean flow variables. Several closure models with one or more equations have been developed. In this study, the turbulence is simulated by the two-equation $SST\ k-\omega$ model (Menter 1994). This model is a combination of the $k-\varepsilon$ and $k-\omega$ models. It uses the $k-\omega$ model near the wall and switches to a $k-\varepsilon$ model away from the wall. The applied equations write as:

$$\frac{\partial k}{\partial t} + u_j \frac{\partial k}{\partial x_j} = P_k - \beta^* k\omega + \frac{\partial}{\partial x_j}\left[(\upsilon + \sigma_k \upsilon_T)\frac{\partial k}{\partial x_j}\right] \tag{9}$$

$$\frac{\partial \omega}{\partial t} + u_j \frac{\partial \omega}{\partial x_j} = \beta S^2 - \alpha\omega^2 + \frac{\partial}{\partial x_j}\left[(\upsilon + \sigma_\omega \upsilon_T)\frac{\partial \omega}{\partial x_j}\right] + 2(1-F_1)\sigma_{\omega 2}\frac{1}{\omega}\frac{\partial k}{\partial x_i}\frac{\partial \omega}{\partial x_i} \tag{10}$$

where k is the turbulent kinetic energy, ω is the specific dissipation rate. More details regarding the definitions of the model parameters can be found in Menter (1994).

This model has been successfully applied in a large number of works relating to the simulation of flow around wind turbines, including the works of Bekhti *et al.* (2016), Karbasian *et al.* (2016),Vučina *et al.* (2016), Ali *et al.* (2019), and many others.

3.2. Discrete Adjoint Formulation

ANSYS Fluent Adjoint Solver is a gradient-based method that uses the discrete adjoint approach (ANSYS 2020). This method aims to compute the gradient (sensitivity) of the objective function, F, with regard to the design parameters, D. The gradient of the objective function is written as

$$\frac{dF}{dD} = \frac{\partial F}{\partial D} + \frac{\partial F}{\partial U}\frac{\partial U}{\partial D} \tag{11}$$

The term $\frac{\partial U}{\partial D}$ is determined using the derivative of the residual vector as follows:

$$\frac{dR}{dD} = \frac{\partial R}{\partial D} + \frac{\partial R}{\partial U}\frac{\partial U}{\partial D} = 0 \tag{12}$$

$$\Rightarrow \frac{\partial U}{\partial D} = -\frac{\partial R}{\partial D}\left[\frac{\partial R}{\partial U}\right]^{-1} \tag{13}$$

Substituting the solution for $\frac{\partial U}{\partial D}$ from Eq. 5 into Eq. 3 to get

$$\frac{dF}{dD} = \frac{\partial F}{\partial D} - \frac{\partial F}{\partial U}\left[\frac{\partial R}{\partial U}\right]^{-1}\frac{\partial R}{\partial D} \tag{14}$$

Then with the introduction of the adjoint vector λ^T, the linear system in equation 6 is defined only by partial derivatives as

$$\frac{dF}{dD} = \frac{\partial F}{\partial D} - \lambda^T\frac{\partial R}{\partial D} \tag{15}$$

The adjoint vector is known by solving the adjoint equation given as follows:

$$\left[\frac{\partial F}{\partial U}\right]^T = \lambda\left[\frac{\partial R}{\partial U}\right]^T \tag{16}$$

For more details or additional information about the discrete Adjoint Solver, the reader is invited to refer to the ANSYS Fluent help (ANSYS 2020).

4. NUMERICAL METHOD

4.1. Flow Field Solver

A pressure-based solver is applied to solve the governing equations. The pressure-velocity coupling was ensured by the coupled algorithm. For the spatial gradient discretization, a Green-Gauss Cell-based approach is applied. The pressure and momentum terms are discretized using the second-ordered scheme and the second-order Upwind method, respectively. The first order Upwind method is used to calculate the turbulent kinetic energy and dissipation rate. For all simulations, maximal numbers of iterations per time step and target residuals for convergence are set to 70 and 10^{-5}, respectively.

4.2. Adjoint Solver

The discrete Fluent Adjoint Solver is based on the specific discretized form of the equations applied in the flow solver (ANSYS 2020). Therefore, the discrete adjoint equation is directly depending on the type of scheme used in the flow solver (Nadarajah and Jameson 2000). Using the same scheme in both the flow solver and the Adjoint Solver leads to enhancement of the adjoint results (ANSYS 2020). Hence, the schemes used in this study for the adjoint solution are a second-order scheme for pressure and momentum, and Green-Gauss Cell-based for the spatial gradient discretization. The turbulence modelling is based on the frozen turbulence assumption. The automatic adjustment is selected to ensure the stability of the adjoint solution. Thereby, the appropriate scheme is automatically selected if a numerical discrepancy is encountered when computing the adjoint solution (Day *et al.* 2021). The morphing zone defined for the optimization ranges between 0 and c in x direction and between -0.25c and 0.25c in y direction. This configuration is chosen to fix the airfoil leading and trailing edges and to maintain the initial angle of attack. The numbers of control points are set to 30 in the x direction and 20 in the y direction. The adjoint equations convergence criterions are set to 0.001, and the adjoint solution iteration limit is set to 1000. The settings used in the Adjoint Solver are summarized in Table 1.

Table 1 Adjoint solver settings.

Objective function	Lift to drag ratio (C_L/C_d)
Target performance change	+50% (of C_L/C_d)
Adjoint solution iteration limit	1000
Adjoint solution stability scheme	Automatic
Geometric constraints	Constant chord length Constant angle of attack
Size of mesh morphing zone as a multiple of chord length	1c in the x direction 0.5c in the y direction
Number of control points in mesh morphing zone	30 in the x direction 20 in y the direction
Freeform Scaling Scheme	Objective reference change
Freeform Scale Factor	1

4.3. Computational Grid and Boundaries Conditions

The computational domain is an O-H type, with an outer sub-domain of length 60c and height 30c. The inner sub-domain that contains the airfoil has a radius of 5c (Fig. 2). This O-H configuration allows the simulation of the flow around an airfoil at different angles of attack without remeshing the computational domain, the internal subdomain only has to be rotated (Moshfeghi and Hur 2017). The inner domain is meshed with a very fine structured grid to accurately compute the physical gradients close to the airfoil surface. To properly solve the boundary layer, the initial grid point is placed at $2.35\ 10^{-5}c$ from the airfoil surface, so that the non-dimensional wall distance y^+ is less than 1.

The outer domain is also meshed with a structured but less dense mesh, to minimize the number of cells and enhance the efficiency of the calculation.

The boundary conditions used in this study are defined as follows (Fig. 2):

- Velocity-inlet condition is prescribed at the inlet, top, and bottom boundaries: the pressure gradient is set to zero and the x-component of the fluid velocity is specified according to the considered Reynolds number.
- At the outlet boundary, a pressure outlet condition is applied: the free stream pressure is imposed and a zero-velocity gradient is assumed.
- At the airfoil surface, a wall no-slip condition is defined.

- The inner and outer sub-domains are connected by conformal interfaces

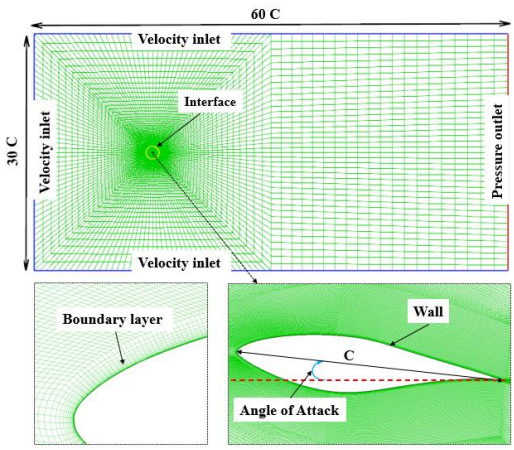

Fig. 2. Mesh and boundary conditions.

4.4. Grid Independency Study

To confirm that the results presented here are not influenced by the grid size, four computational grids with different mesh densities are considered: a coarse mesh built with 21600 cells, a medium mesh built with 31100 cells, a fine mesh composed of 61850 cells and a very fine mesh of 126300 cells. Numerical simulations are performed for an S809 airfoil of 1m chord, at an angle of attack of 6.1°, in a flow at a Reynolds number of 10^6. Figure 3 shows the pressure coefficient distribution around the airfoil surface calculated with the different grids, compared to the experimental data of (Ramsay *et al.* 1995). The results obtained with the fine and very fine meshes are similar and fit better with experimental data. As increasing the number of cells does not improve the results, the fine grid is applied for the following computations.

4.5. Validation

To check the accuracy of the used CFD model, computations of the flow field around the S809 airfoil at various angles of attack from 0° to 20° are conducted. The obtained lift and drag coefficients are depicted in Fig. 4 compared to experimental data published by (Ramsay *et al.* 1995) and (Somers 1997). The results are also compared to the numerical results obtained for the same flow configuration by Johansen (1999) and Zhong *et al.* (2017). It can be seen that the current computational results correspond well to the experiments up to an angle of attack of about 9°. At larger angles (> 9°), the difference with experimental data is remarkable. This difference, which has been observed in many works (Wang *et al.* 2017; Shi *et al.* 2019; Rodriguez and Celis 2022), can be attributed to the accuracy of the turbulence models, which are less accurate in predicting lift and drag coefficients beyond the stall angle. Moreover, as shown in Fig. 4, the experimental results of (Ramsay *et al.* 1995) and (Somers 1997) are different especially in the region

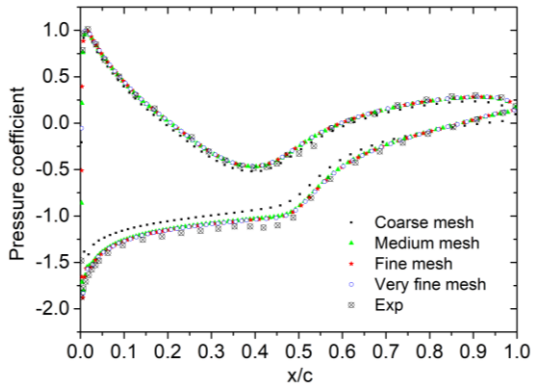

Fig. 3. Pressure coefficient distribution over airfoil surface for tested meshes compared to experimental data, at $AoA = 6.1°$ and $Re = 10^6$.

of large angles of attacks (>18°). According to Ge *et al.* (2019), this difference is due to the experimental circumstances, including the inflow turbulence intensity, the airfoil surface, and the precision of the measuring tools utilized in both cases. Nevertheless, at all angles of attacks, the current computational results are in good agreement with the published computational results. These results confirm that the present RANS solver can calculate the aerodynamics around the S809 airfoil. Furthermore, in this study, the angle of attack considered for the design optimization is 6.1°, corresponding to the zone where our results agree well with the experimental data.

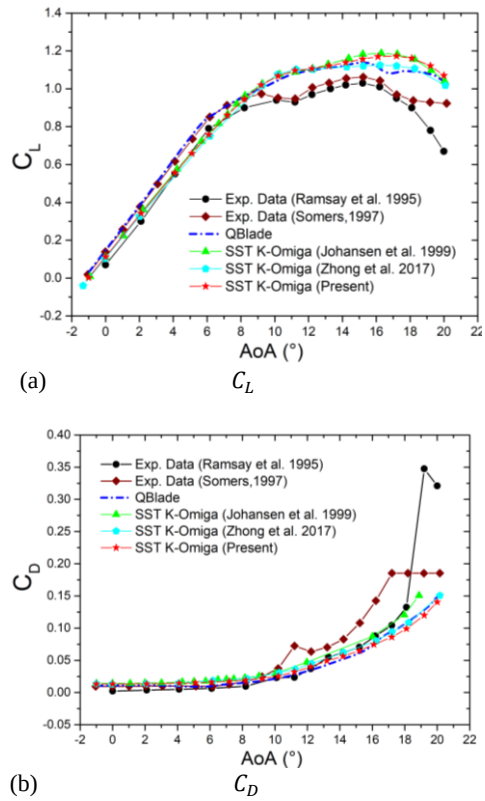

Fig. 4. Lift (a) and drag (b) coefficients versus angle of attack at $Re = 10^6$.

5. RESULTS AND DISCUSSION

5.1. Airfoil Shape Optimization

The optimization process is applied to the S809 airfoil set at 6.1° angle of attack. Three Reynolds numbers are considered for the fluid flow computations, $Re = 3\ 10^5, 4.8\ 10^5$ and 10^6. The objective function was set to increase the target lift to drag ratio by 50% of the nominal lift to drag ratio. The leading and trailing edge points are kept fixed during the optimization process. Therefore, the airfoil chord and the angle of attack do not change after the deformation. The airfoils obtained after convergence of the optimization process are named Optimized A (for Re = $3\ 10^5$), Optimized B (for Re = $4.8\ 10^5$), and Optimized C (for Re = 10^6). These airfoils are depicted in Fig. 5, compared to the reference S809 airfoil. Table 2 shows that the optimized airfoil shape varies depending on the operating conditions: the thickness, maximum thickness position, camber and maximum camber position are different. It can be seen that the maximum thickness of the optimized airfoils is reduced and the position of the maximum thickness shifts towards the leading edge, which leads to an expected reduction in drag force. Concerning the camber, the maximum camber of the optimized airfoils is increased and the maximum camber position is shifted towards the leading edge, which helps to enhance the lift. Consequently, these changes in the shape of the airfoil increase in the lift to drag ratio. The aerodynamic coefficients of the three optimized airfoils are presented in Table 3 compared to those of the reference airfoil. These results show that, regardless of the Reynolds number, the optimized airfoils have higher lift coefficients and C_L/C_D ratios than the reference S809 airfoil. The lift to drag ratio of the optimized airfoils is enhanced by 46.27%, 38.48%, and 24.99% for the Optimized A, Optimized B, and Optimized C airfoils respectively, compared to the baseline S809 airfoil.

To explain the higher performances of the new profiles, the distributions of the pressure coefficients, the pressure contours, and the turbulent kinetic energy contours are represented in Figures 6 to 11 for the three optimized airfoils and the baseline airfoil. Figures 6, 7 and 8 which represent pressure distributions and pressure contours, show that over 60% of the airfoil surface from the leading edge, the pressure differences between the upper and lower surfaces of the optimized profiles are greater than those of the reference airfoil. Due to these higher-pressure differences, a higher lift is generated by the optimized airfoils compared to the reference airfoil. The turbulent kinetic energy contours depicted in

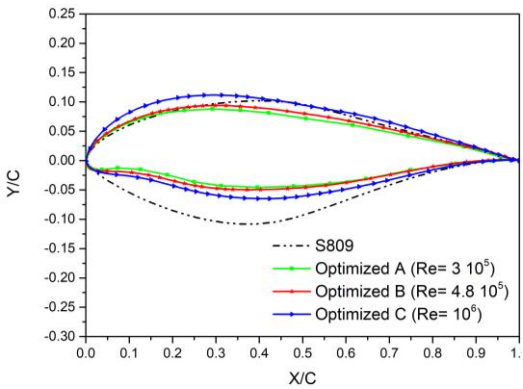

Fig. 5. Original and optimized airfoil shapes for different Reynolds numbers.

Table 2 Geometric parameters of original and optimized airfoils.

Geometric characteristics	Airfoils			
	S809	Optimized A	Optimized B	Optimized C
Max. Thickness (%)	20.99	13.02	14.24	17.33
Max. Thickness position (%)	38.30	31.30	33.09	35.31
Max. Camber (%)	0.99	2.91	2.75	3.21
Max. Camber position (%)	82.30	17.30	16.49	16.71

Table 3 Performance comparison of original and optimized airfoils at 6.1°.

Airfoils	S809	Optimized A	S809	Optimized B	S809	Optimized C
Re	$3\ 10^5$		$4.8\ 10^5$		10^6	
C_L	0.685	0.863	0.722	0.914	0.752	0.932
C_D	0.021	0.018	0.018	0.017	0.016	0.016
C_L/C_D	32.400	47.393	38.625	53.491	45.870	57.334
C_L/C_D Improvement		46.274 %		38.488%		24.992%

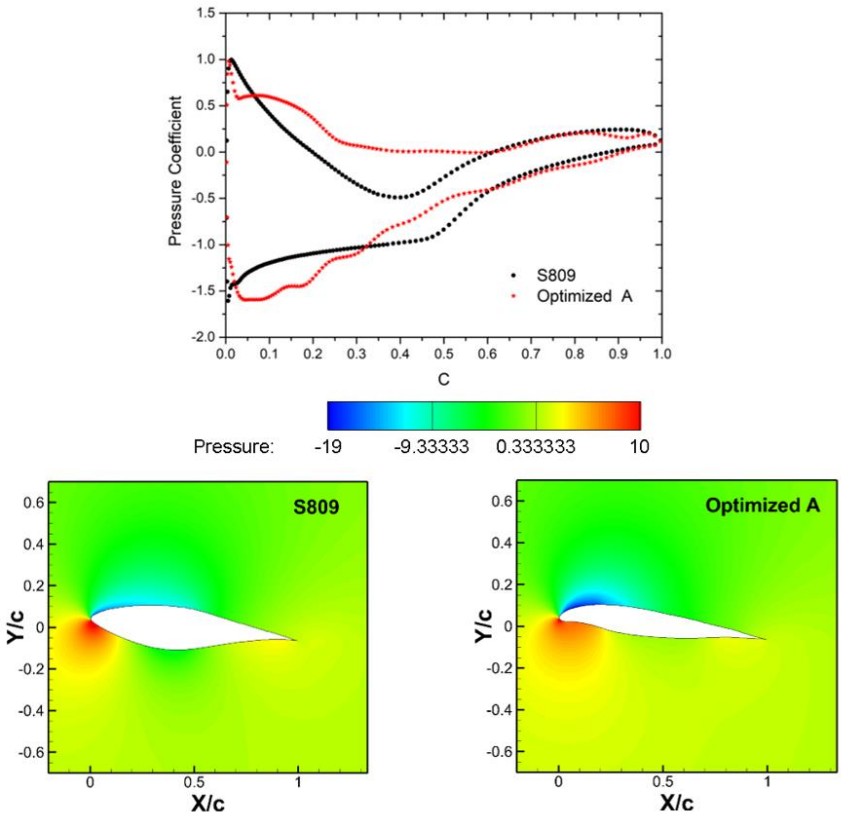

Fig. 6. Pressure coefficient and contours of pressure around the reference and optimized A airfoils.

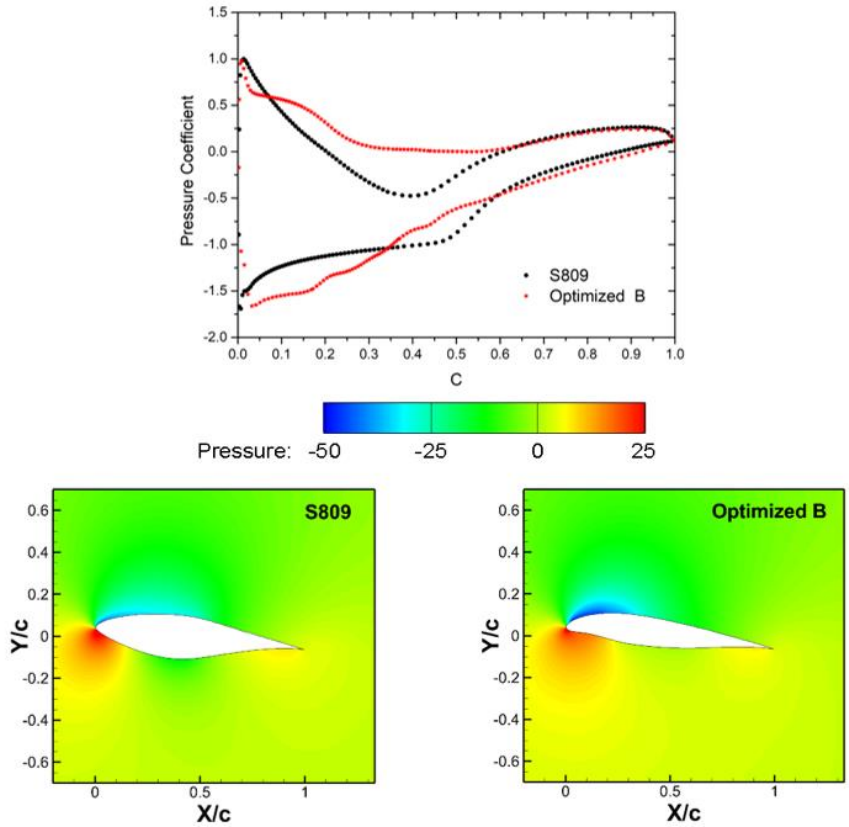

Fig. 7. Pressure coefficient and contours of pressure around the reference and optimized B airfoils.

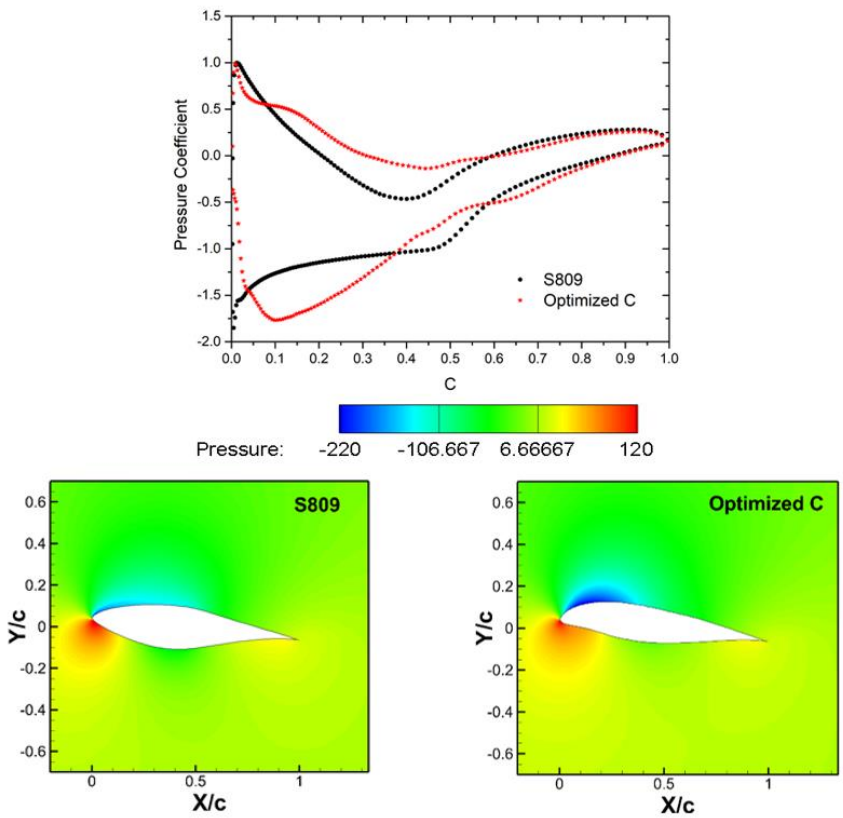

Fig. 8. Pressure coefficient and contours of pressure around the reference and optimized C airfoils.

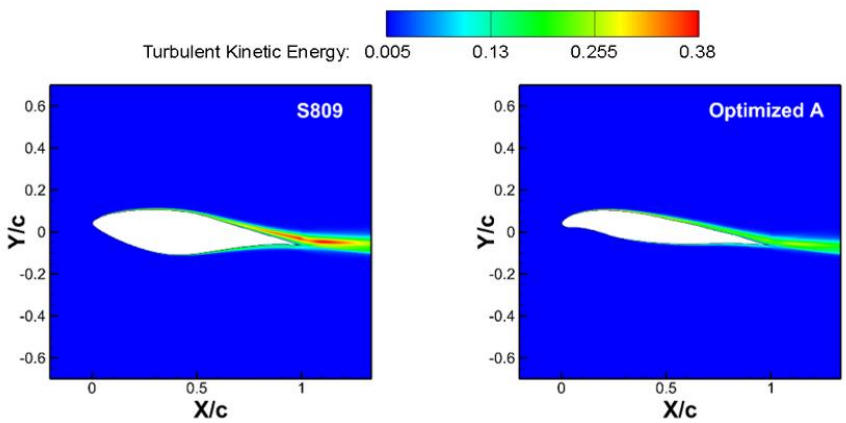

Fig. 9. Contours of turbulent kinetic energy around the reference and optimized A airfoils.

Figs. 9 and 10 reveal that less turbulent kinetic energy is generated in the wake of the optimized A and optimized B airfoils, compared to the reference S809 profile. The friction drag is therefore lower as indicated in Table 3. However, the contours of the turbulent kinetic energy around the optimized C profile and the S809 profile seem similar (Fig. 11). As shown in Table 3, the resulting drag coefficients are equal for both airfoils. This could be because the Reynolds number specified for this case matches the Reynolds number considered for the design of the S809 reference airfoil. Yet, in all cases, the optimized airfoils exhibited higher lift to drag ratios than the baseline airfoil (Table 3).

5.2. Angle of attack effect

Numerical simulations are performed to determine the aerodynamic coefficients of the optimized airfoils over a wide range of angles of attack (AOA).

These computations are carried out for AOAs varying from 0° to 20° and for the three Reynolds numbers considered. The obtained results depicted in

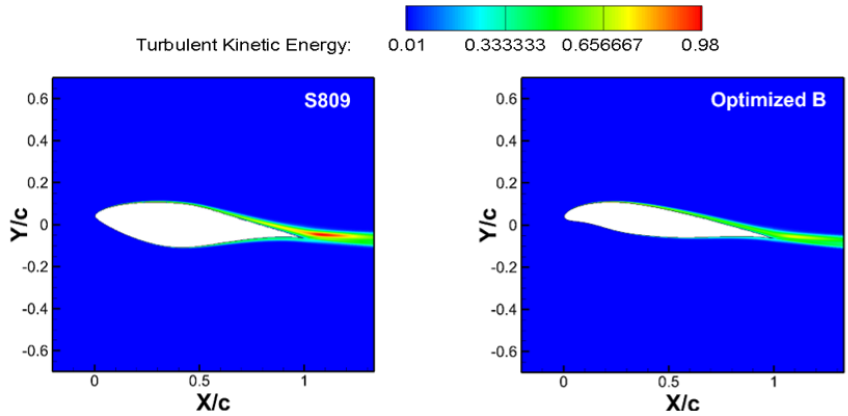

Fig. 10. Contours of turbulent kinetic energy around the reference and optimized B airfoils.

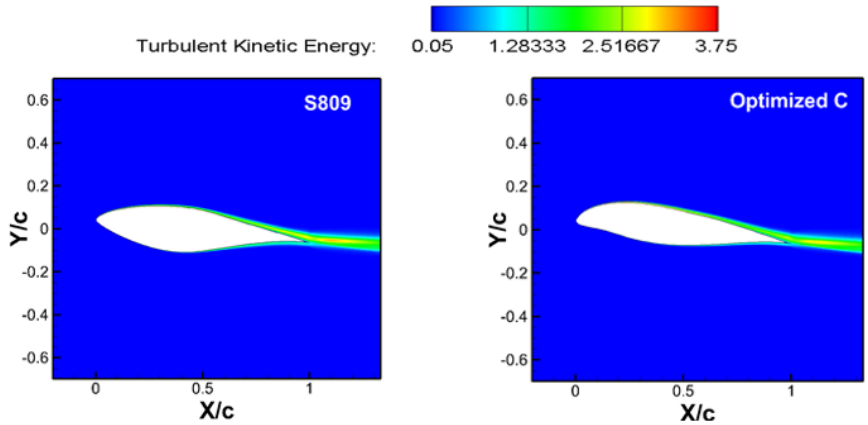

Fig. 11. Contours of turbulent kinetic energy around the reference and optimized C airfoils.

Figs. 12, 13 and 14 show that the aerodynamic characteristics of the optimized airfoils outperform those of the reference airfoil when the AoA is less than 14°. However, beyond this angle and in particular when the AoA is between 14° and 18°, the C_L and C_L/C_D values of the optimized profiles are lower, those of the drag are higher. This may be caused by the static stall that occurs earlier. Indeed, as can be seen in these Figures, the stall angle of the optimized airfoils is approximately 12°, whereas for the reference airfoil, the static stall occurs at 15°. On the other hand, these Figures show that the maximum values of the lift to drag ratio are obtained at the same angle of attack AoA = 6.1° for all the profiles, i.e both for the reference airfoil and for the optimized airfoils.

5.3. Reynolds number effect

To corroborate the above results, the influence of the Reynolds number on the aerodynamic characteristics of the optimized airfoils is studied. Figure 15 shows

the aerodynamic coefficients of the reference and optimized airfoils set at 6.1° angle of attack computed for four Reynolds numbers, $Re = 3\ 10^5$, $Re = 4.8\ 10^5$, $Re = 10^6$ and $Re = 2\ 10^6$. It can be seen that, for all airfoils, the lift coefficient and the lift to drag ratio rise as the Reynolds number increases, whereas the drag coefficient decreases as the Reynolds number increases. Likewise, for the considered Reynolds numbers, the optimized airfoils show better performances compared to those of the original airfoil. In addition, the aerodynamic performance of the optimized B airfoil is better than to that of the optimized A and optimized C airfoils. At $Re = 2\ 10^6$, the lift coefficient of the Optimized B airfoil is increased by 23.81% and the drag coefficient is reduced by 7.18%. The resulting improvement in lift to drag ratio is 33.39%.

5.4. Comparison with other optimization methods

The results obtained with the present technique based on the discrete Adjoint Solver of Fluent are compared to those of Akram and Kim (2021) who have applied two optimization methods, the class shape transformation (CST) and the parametrization method of parametric section (PARSEC), coupled with the genetic algorithm. The airfoil shapes obtained with the two studies are depicted in Fig. 16 which shows that the maximum thickness of the optimized CST and PARSEC

airfoils is retained, compared to the baseline airfoil. This parameter was imposed as a constraint by Akram and Kim (2021), it was not retained in the current investigations. The aerodynamic coefficients of the current optimized A, B and C airfoils are then calculated for a Reynolds number of 7.5 10^5 and an effective angle of attack of 6.2°, for comparison with the published results.

Table 4 shows the C_L, C_D and C_L/C_D values obtained for the current optimized airfoils as well as the CST and PARSEC airfoils whose values were computed by Akram and Kim (2021). It can be seen that the aerodynamic characteristics of the three optimized airfoils A, B, and C are similar to those of the optimized PARSEC airfoil, with relative errors varying between 3.4% to 6.9% for the C_L coefficient and -8.5% to +0.1% for the C_L/C_D ratio. The airfoil drag obtained with the CST method is lower than that of the currently optimized airfoil, resulting in a higher lift to drag ratio. As for the CPU time, the optimization process requires 210 minutes for the CST and 272 minutes for the PARSEC method Akram and Kim (2021). With the applied adjoint solver technique, the airfoil optimizations are performed in less than 30 minutes. The methods based on the genetic algorithm are then more expensive in terms of computational time compared to the current technique based on the discrete adjoint solver.

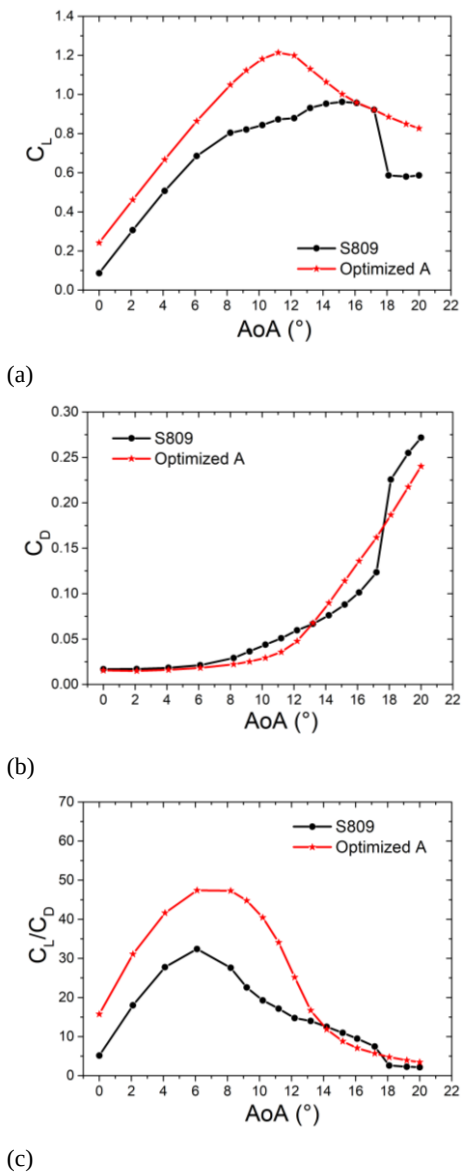

Fig. 12. Aerodynamic coefficients of the original and Optimized A airfoils at various AoAs. (a) Lift coefficient, (b) Drag coefficient and (c) lift to drag ratio.

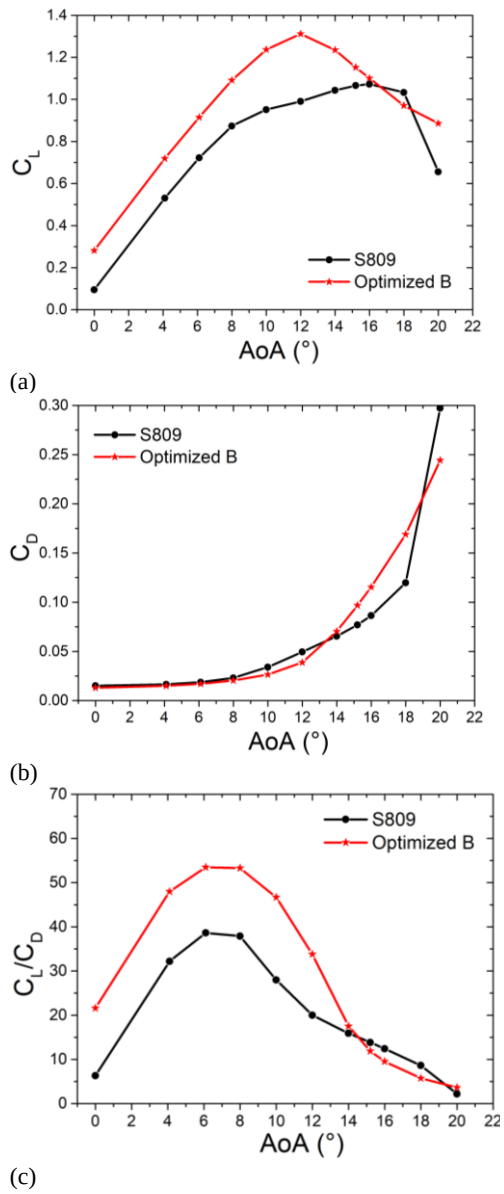

Fig. 13. Aerodynamic coefficients of the original and Optimized B airfoils at various AoAs. (a) Lift coefficient, (b) Drag coefficient and (c) lift to drag ratio.

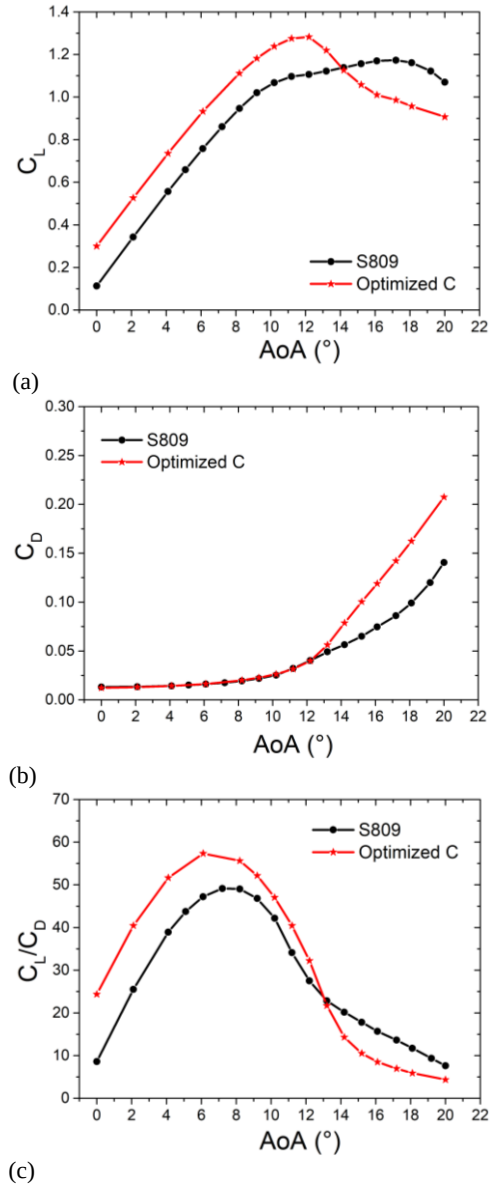

Fig. 14. Aerodynamic coefficients of the original and Optimized C airfoils at various AoAs. (a) Lift coefficient, (b) Drag coefficient and (c) lift to drag ratio.

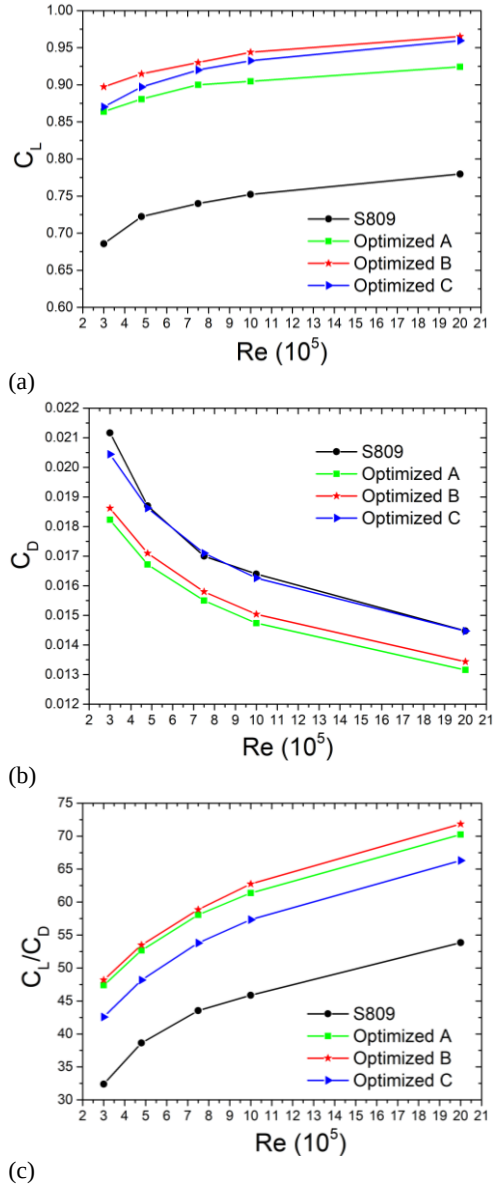

Fig. 15. Aerodynamic coefficients of the original and Optimized airfoils as a function of the Reynolds number Re at various AoAs, $Re = 10^6$. (a) Lift coefficient, (b) Drag coefficient and (c) lift to drag ratio.

Table 4 Airfoil coefficients optimized in this study and optimized by Akram and Kim (2021).

	Present results				(Akram and Kim 2021)	
	S809	Optimized A	Optimized B	Optimized C	Optimized CST	Optimized PARSEC
C_L	0.74	0.90	0.93	0.92	0.883	0.87
C_D	0.017	0.0155	0.0158	0.0171	0.013	0.015
C_L/C_D	43.53	58.06	58.86	53.8	65.9	58.8

5.5. Performance enhancement of the wind turbine

The results obtained suggest that improvements in the power output of wind turbines made with these optimized airfoils are expected. Therefore, a study on wind turbine performance improvements using the optimized airfoils is applied to the NREL Phase VI wind turbine whose main operating parameters are summarized in table 5. The reference blade is designed with the S809 airfoil, and three new blades are designed with the optimized airfoils (Optimized A, Optimized B, and Optimized C). Distributions

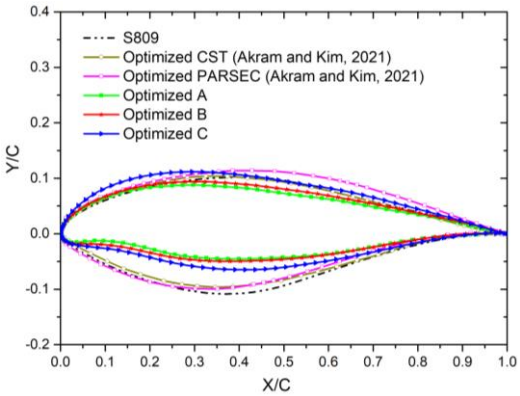

Fig. 16. Airfoil shapes obtained by this study and by Akram and Kim (2021).

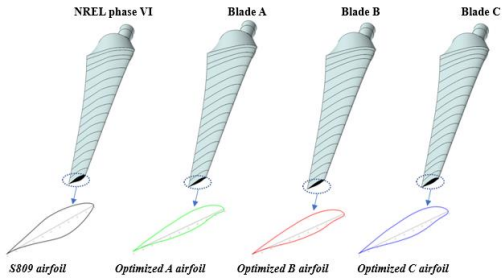

Fig. 17. Geometric representation of the original S809 and optimized blades.

along the span of the twist angle and chord are those of the NREL phase VI wind turbine blade (Simms *et al.* 1999), the only difference is the airfoil shape (Fig. 17).

The wind turbine performances are computed using the software Qblade, an open-source framework dedicated to the design and performance assessment of wind turbines, based on the Blade Element Momentum (BEM) method. 3D corrections of the airfoil characteristics are applied using the Viterna method (Viterna and Janetzke 1982).

The characteristic curves depicted in Fig. 18 show that the power coefficients of the optimized rotors are higher than that of the reference turbine when the TSR is less than 7, while a small difference in power coefficients is noticed for TSR values larger than 7.

The optimized blades have almost the same C_P curves, with a slight advantage for the optimized blade B. The reference wind turbine has a maximum power coefficient of 0.39 at the TSR = 7, while the optimized rotors have a maximum power coefficient of 0.43 and the corresponding TSR is 6. This indicates that optimal wind turbine operation with optimized blades would require higher wind speeds or lower rotational speeds.

The power curves of the original and optimized wind turbine are depicted in Fig. 19 showing that the expected power of the optimized rotors is improved throughout all wind speeds.

Table 5 Operating condition of the NREL Phase VI wind turbine.

Parameters	Value
Rated power	19.8 kW
blade radius	5.024 m
Number of blades	2
Pitch angle	3°
Rotational speed	71.63 rpm
Power regulation	Stall

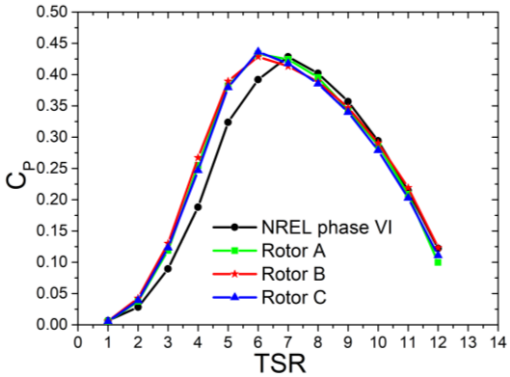

Fig. 18. Power coefficient versus TSR for original and optimized blades.

At wind speeds less than or equal to 6 m/s, the reference and optimized wind turbine rotors have almost the same power output, while at higher wind speeds, above 10 m/s, the output power of the optimized rotors is greatly improved compared to the reference rotor. At 10 m/s wind speed, the output power of the A, B and C rotors are improved by 30.45%, 37.42% and 27.14%, respectively compared to the reference NREL phase VI turbine (Table 6).

Table 6 Power output of the original and optimized rotors at 10m/s.

Rotors	Power (W)	Impro (%)
NREL phase VI	9.69	--
Rotor A	12.64	30.45
Rotor B	13.31	37.42
Rotor C	12.32	27.14

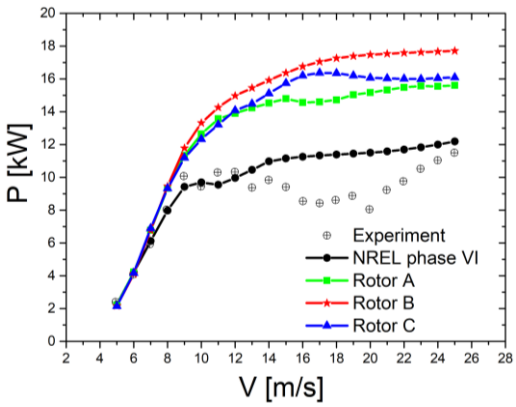

Fig. 19. Power performance of the original and the optimized rotors.

6. CONCLUSION

In the present study, airfoil shape optimization is performed using CFD and the discrete adjoint approach to maximize the lift to drag ratio of wind turbine airfoils and to improve wind turbine performance. The simulations are carried out with the industrial code ANSYS Fluent. In the flow solver, the turbulence is modeled by the SST k-ω model and in the adjoint solver the frozen turbulence assumption is applied. The S809 airfoil and NREL Phase VI wind turbine are used as the reference airfoil and turbine. The main findings of this study are summarized as follows:

- Optimization performed using the Adjoint Solver resulted in significant improvements in the aerodynamic characteristics of the optimized airfoils compared to the reference airfoil.
- The optimal airfoil shape obtained for the same airfoil at various wind speeds is different.
- Optimized airfoils are thinner than the reference S809 airfoil. Therefore, they can be used for the design of small scale HAWT.
- Using the same chord and twist distributions, the wind turbines with blades based on the optimized airfoils have higher performances compared to the reference wind turbine, this is reflected in a higher power coefficient and power output.

These results show that the adjoint solver approach can be directly applied to blade design to improve the efficiency of wind turbines. Compared to other techniques such as methods based on genetic algorithms, the applied discrete adjoint solver technique is much less CPU intensive.

7. FUTURE WORKS

The blades of today's wind turbines are increasingly large, light, and flexible, which introduces aeroelastic effects. In addition, there is a trend towards the use of composite materials for their manufacture. Therefore, optimizing aerodynamic performance is not enough. Structural optimization and aeroelasticity must be taken into account. Structural optimization determines the optimal layering of the composite material to minimize the blade's mass while fulfilling the design constraints (Sale *et al.* 2013). As for aeroelasticity, its effects can lead to instability problems that can be harmful to the blades and the turbine (Wang *et al.* 2016). Effective approaches to aeroelasticity analysis involve coupling CFD with a structural solver (Guma *et al.* 2021). These other topics are being investigated and will be the subject of future articles.

ACKNOWLEDGEMENTS

The authors of the manuscript gratefully acknowledge the Centre de Développement des Energies Renouvelables of Algiers (CDER), for providing all the necessary resources to achieve this study.

REFERENCES

Akram, M. T. and M. H. Kim (2021). Aerodynamic Shape Optimization of NREL S809 Airfoil for Wind Turbine Blades Using Reynolds-Averaged Navier Stokes Model—Part II. *Applied Sciences* 11(5), 2211.

Ali, B., G. Ouahiba, O. Hamid and B. Ahmed (2019). Aerodynamic optimization of active flow control over S809 airfoil using synthetic jet. In *2018 International Conference on Wind Energy and Applications in Algeria*, IEEE.

ANSYS Fluent User's Guide, Release 2020 R2.

Bekhti, A., O. Guerri and T. Rezoug (2016). Flap/lead-lag computational investigations on NREL S809 airfoil. *Mechanics and Industry* 17(6), 606.

Chen, J., Q. Wang, S. Zhang, P. Eecen and F. Grasso (2016). A new direct design method of wind turbine airfoils and wind tunnel experiment. *Applied Mathematical Modelling* 40(3), 2002-2014.

Day, H., D. Ingham, L. Ma and M. Pourkashanian (2021). Adjoint based optimisation for efficient VAWT blade aerodynamics using CFD. *Journal of Wind Engineering and Industrial Aerodynamics* 208, 104431.

Derakhshan, S., A. Tavaziani and N. Kasaeian (2015). Numerical shape optimization of a wind turbine blades using artificial bee colony algorithm. *Journal of Energy Resources Technology, Transactions of the ASME* 137(5).

Dhert, T., T. Ashuri and J. R. R. A. Martins (2017). Aerodynamic shape optimization of wind turbine blades using a Reynolds-averaged Navier–Stokes model and an adjoint method. *Wind Energy* 20(5), 909-926.

Ge, M., H. Zhang, Y. Wu and Y. Li (2019). Effects of leading edge defects on aerodynamic performance of the S809 airfoil. *Energy Conversion and Management* 195, 466-479.

Grasso, F. (2012). Hybrid optimization for wind turbine thick airfoils. In *Collection of Technical Papers - AIAA/ASME/ASCE/AHS/ASC Structures, Structural Dynamics and Materials Conference*.

Guma, G., G. Bangga, T. Lutz and E. Krämer (2021). Aeroelastic analysis of wind turbines under turbulent inflow conditions. *Wind Energy Science* 6(1), 93-110.

He, Y. and R. K. Agarwal (2014). Shape Optimization of NREL S809 Airfoil for Wind Turbine Blades Using a Multiobjective Genetic Algorithm. *International Journal of Aerospace Engineering*.

Johansen, J. (1999). *Unsteady Airfoil Flows with Application to Aeroelastic Stability*. Technical University of Denmark.

Kamali Moghadam, R., H. Jalali and A. Haghiri

(2020). Wave drag reduction of SC(2)0410 airfoil using new developed inviscid compressible adjoint method. *Journal of Applied Fluid Mechanics* 13(4), 1277-1287.

Karbasian, H. R., J. A. Esfahani and E. Barati (2016). Effect of acceleration on dynamic stall of airfoil in unsteady operating conditions. *Wind Energy* 19(1), 17-33.

Khalil, Y., L. Tenghiri, F. Abdi and A. Bentamy (2020). Improvement of aerodynamic performance of a small wind turbine. *Wind Engineering* 44(1), 21-32.

Li, H. C., Z. M. Yang, L. Zhang and R. Li (2021). Adjoint optimization method for head shape of high- speed maglev train. *Journal of Applied Fluid Mechanics* 14(6), 1839-1850.

Li, J. Y., R. Li, Y. Gao and J. Huang, (2010). Aerodynamic optimization of wind turbine airfoils using response surface techniques. *Proceedings of the Institution of Mechanical Engineers, Part A: Journal of Power and Energy* 224(6), 827-838.

Li, S., Y. Li, C. Yang, X. Zhang, Q. Wang, D. Li, W. Zhong and T. Wang (2018). Design and testing of a lut airfoil for straight-bladed vertical axis wind turbines. *Applied Sciences* 8(11), 2266.

Menter, F. R. (1994). Two-equation eddy-viscosity turbulence models for engineering applications. *AIAA Journal* 32(8), 1598-1605.

Moshfeghi, M. and N. Hur (2017). Numerical study on the effects of a synthetic jet actuator on S809 airfoil aerodynamics at different flow regimes and jet flow angles. *Journal of Mechanical Science and Technology* 31(3), 1233-1240.

Munoz-Paniagua, J., J. García, A. Crespo and F. Laspougeas (2015). Aerodynamic optimization of the nose shape of a train using the adjoint method. *Journal of Applied Fluid Mechanics* 8(3), 601-612.

Nadarajah, S. K. and A. Jameson (2000). A comparison of the continuous and discrete adjoint approach to automatic aerodynamic optimization. In *38th Aerospace Sciences Meeting and Exhibit*, Reno, NV,U. S. A.

Perez-Blanco, H. and M. McCaffrey (2013). Aerodynamic performance of preferred wind turbine airfoils. *Proceedings of the ASME Turbo Expo* 6, 743-752.

Ramsay, R., Hoffman, M., and Gregorek, G. (1995). *Effects of Grit Roughness and Pitch Oscillations on the S809 Aerofoil. NREL/TP-442-7817*, National Renewable Energy Laboratory, Golden, CO.

Ribeiro, A. F. P., A. M. Awruch and H. M. Gomes (2012). An airfoil optimization technique for wind turbines. *Applied Mathematical Modelling* 36(10), 4898-4907.

Rodriguez, C. V. and C. Celis (2022). Design optimization methodology of small horizontal axis wind turbine blades using a hybrid CFD/BEM/GA approach. *Journal of the Brazilian Society of Mechanical Sciences and Engineering* 44(6), 254.

Sale, D., A. Alberto, M. Michael and Y. Li (2013). Structural optimization of composite blades for wind and hydrokinetic turbines. In *Proceedings 1 St Marine Energy Technology Conference*, Washington.

Schramm, M., B. Stoevesandt and J. Peinke (2018). Optimization of airfoils using the adjoint approach and the influence of adjoint turbulent viscosity. *Computation* 6(1), 5.

Shi, X., S. Xu, L. Ding and D. Huang (2019). Passive flow control of a stalled airfoil using an oscillating micro-cylinder. *Computers and Fluids* 178, 152-165.

Simms, D. A., M. M. Hand, L. J. Fingersh and D. W. Jager (1999). *Unsteady Aerodynamics Experiment Phases II-IV Test Configurations and Available Data Campaigns*. National Renewable Energy Lab. Golden, CO (United States).

Somers, D. M. (1997). *Design and Experimental Results for the S809 Airfoil*. Nat Renew Energy Lab.

Tahani, M., G. Kavari, M. Masdari and M. Mirhosseini (2017). Aerodynamic design of horizontal axis wind turbine with innovative local linearization of chord and twist distributions. *Energy* 131, 78-91.

Timmer, W. A. and R. P. J. O. M. Van Rooij (2003). Summary of the delft university wind turbine dedicated airfoils. *Journal of Solar Energy Engineering* 125(4), 488-496.

Viterna, L. A. and D. C. Janetzke (1982). *Theoretical and Experimental Power from Large Horizontal-Axis Wind Turbines*. National Aeronautics and Space Administration, Cleveland, OH (USA). Lewis Research Center.

Vučina, D., I. Marinić-Kragić and Z. Milas (2016). Numerical models for robust shape optimization of wind turbine blades. *Renewable Energy* 87, 849-862.

Wang, H., B. Zhang, Q. Qiu and X. Xu (2017). Flow control on the NREL S809 wind turbine airfoil using vortex generators. *Energy* 118, 1210-1221.

Wang, L., X. Liu and A. Kolios (2016). State of the art in the aeroelasticity of wind turbine blades: Aeroelastic modelling. *Renewable and Sustainable Energy Reviews* 64, 195-210.

Xudong, W., W. Z. Shen, W. J. Zhu, J. N. Sørensen and C. Jin (2009). Shape optimization of wind turbine blades. *Wind Energy* 12(8), 781-803.

Zhong, J., J. Li and P. Guo (2017). Effects of leading-edge rod on dynamic stall performance of a wind turbine airfoil. *Proceedings of the Institution of Mechanical Engineers, Part A: Journal of Power and Energy* 231(8), 753-769 .